MNRAS **000**, 1–9 (2015) Preprint 18 February 2021 Compiled using MNRAS LATEX style file v3.0

Parameters of the eclipsing binary α Draconis observed by *TESS* and *SONG*

Daniel R. Hey,[1,2]★ Angela Kochoska,[3] Richard Monier,[4] Oleg Kochukhov,[5] Cole Johnston, [6,7] Timothy R. Bedding,[1,2] Simon J. Murphy,[1,2] Michael Abdul-Masih,[8] John Southworth,[9] Mads Fredslund Andersen,[2] Frank Grundahl,[2] and Pere L. Pallé [10]

[1] *School of Physics, Sydney Institute for Astronomy (SIfA), The University of Sydney, NSW 2006, Australia*
[2] *Stellar Astrophysics Centre, Department of Physics and Astronomy, Aarhus University, DK-8000 Aarhus C, Denmark*
[3] *Department of Astrophysics and Planetary Science, Villanova University, 800 East Lancaster Avenue, Villanova, PA 19085, USA*
[4] *LESIA, UMR 8109, Observatoire de Paris et Université Pierre et Marie Curie Sorbonne Universités, place J. Janssen, Meudon, France*
[5] *Department of Physics and Astronomy, Uppsala University, Box 516, SE-75120 Uppsala, Sweden*
[6] *Institute of Astronomy, KU Leuven, Celestijnenlaan 200D, 3001 Leuven, Belgium*
[7] *Department of Astrophysics, IMAPP, Radboud University Nijmegen, P. O. Box 9010, 6500 GL Nijmegen, the Netherlands*
[8] *European Southern Observatory, Alonso de Cordova 3107, Vitacura, Casilla 19001, Santiago de Chile, Chile*
[9] *Astrophysics Group, Keele University, Staffordshire, ST5 5BG, UK*
[10] *Instituto de Astrofísica de Canarias, E-38200 La Laguna, Tenerife, Spain*

Accepted XXX. Received YYY; in original form ZZZ

ABSTRACT

We present an analysis of the eclipsing single-lined spectroscopic binary system α Dra based on photometry from the *TESS* mission and newly acquired spectroscopic measurements. Recently discovered to have eclipses in the *TESS* data, at a magnitude of $V = 3.7$, α Dra is now one of the brightest detached eclipsing binary systems known. We obtain the parameters of this system by simultaneously fitting the *TESS* light curve in conjunction with radial velocities acquired from the *SONG* spectrograph. We determine the fractional radii (R/a) for the primary and secondary components of the system to be 0.0479 ± 0.0003 and 0.0226 ± 0.0005 respectively. Although the secondary is too faint to appear in the spectra, we constrain the temperature, mass, and log luminosity of the primary to be 9975 ± 125 K, 3.5 ± 0.1 $M_\odot$, and 2.39 ± 0.03 $L_\odot$ respectively. From the obtained mass function and measured inclination, we find the secondary to have a minimum mass of around $M_2 = 2.5 \pm 0.1$ $M_\odot$, which suggests that it is an A2V type star. We were unable to obtain radial velocities of the secondary, and are only able to see a weak highly rotationally broadened absorption line, indicating that the secondary is rapidly rotating ($v \sin i \sim 200$ km/s). We further perform an abundance analysis of the primary and find mild under-abundances for most elements, in particular helium and iron, which reinforces the metal-deficient status of α Dra. We make available the Python code used in this paper to facilitate future modelling of eclipsing binaries.

Key words: binaries: eclipsing – stars: chemically peculiar – stars: fundamental parameters

1 INTRODUCTION

Eclipsing binaries (EBs) are fundamental to modern astrophysics. They offer an accurate, unbiased method for determining stellar parameters with high precision, and are our primary source of empirical measurements of the masses and radii of normal stars (Andersen 1991; Torres et al. 2010). From light and radial velocity (RV) curves, the masses and radii can be determined to high accuracy Maxted et al. (2020), then used to check and calibrate theoretical models, or as distance indicators (Graczyk 2003).

α Draconis (Thuban; HR 5291; TIC 165991532, hereafter, α Dra) is a well-studied single-lined spectroscopic binary (SB1). Recent observations by the Transiting Exoplanet Survey Satellite (*TESS*) showed that α Dra exhibits clear grazing eclipses that had previously gone unnoticed (Bedding et al. 2019). With knowledge of α Dra predating modern civilization, the recent discovery of eclipses is quite remarkable and highlights the advantage of continuous space-based photometric monitoring. In fact, α Dra has been closely studied in the literature since at least Campbell & Cur-

★ E-mail: daniel.hey@sydney.edu.au

tis (1903). This is largely a result of its brightness: at V = 3.68 magnitude α Dra is easily visible with the naked eye. α Dra is metal-deficient and belongs to the rare class of A0 III stars, with an apparent minor enhancement of Si and Cr (Renson & Manfroid 2009). α Dra is one of the most well-known of the A0 III spectral type (the other being α Sextantis) to the point that it serves as a standard MK class star. With only two other A0 III stars known to exist in an eclipsing system, α Dra provides a near ideal environment to study this spectral type.

In this paper, we analyse *TESS* photometry and simultaneous high-resolution spectroscopic measurements taken with the Stellar Observations Network Group (*SONG*) spectrograph (Sec. 2). We characterise the system using the eclipsing binary software ELLC to obtain precise fractional radii (Sec. 3). Finally, we perform an abundance analysis on archival spectra, confirming the metal-deficient nature of α Dra (Sec. 4).

2 OBSERVATIONS

2.1 TESS photometry

The NASA Transiting Exoplanet Survey Satellite (*TESS*; Ricker et al. 2014) is an all-sky photometric survey satellite whose primary mission is to discover Earth-sized transiting exoplanets. *TESS* has four cameras which cover a combined field of view of 24° by 96° that extends from the ecliptic pole to the ecliptic plane. It has surveyed both ecliptic hemispheres each for one year in 13 sectors. Each sector is observed for around 27 d. Since there is some overlap between sectors, some stars were observed during multiple sectors, especially if they lie close to the ecliptic pole.

TESS observed α Dra at 2-min cadence in five non-contiguous sectors: 14, 15, 16, 21, and 22. We downloaded the target pixel files from the Mikulski Archive for Space Telescopes (MAST), and extracted a simple aperture photometry (SAP) light curve by summing up the flux from each pixel contained within the default aperture mask. We did not make use of the *TESS* pipeline, which provides automatically extracted and cleaned light curves (Pre-Search Data Conditioning; Smith et al. 2012), since it is known to cause anomalous peaks when correcting the light curves of detached eclipsing binaries. Instead, we corrected our light curve with a spline of degree 5 fitted individually to the out-of-eclipse regions of each sector. We then interpolated the spline fit across the entire light curve, eclipses included, and corrected and normalised the light curve. We removed 3σ outliers prior to the spline fit. We show these corrections and the final light curve in Fig. 1 as well as the *TESS* aperture mask used to obtain the light curve.

2.2 High-resolution spectroscopy

We obtained 61 high resolution spectra of α Dra using the *SONG* spectrograph mounted on the 1.0 m robotic Hertzsprung *SONG* telescope at the Teide Observatory in Tenerife (Andersen et al. 2014, 2019). The *SONG* spectrograph is a high resolution échelle spectrograph operating in the wavelength range of 4400-6900 Å. Several exposures were obtained during primary eclipse and one during secondary, to explore any potential Rossiter-McLaughlin effects present in the system. All exposures were obtained at the highest resolution (R = 110,000). The orbital phases at which spectra were obtained is shown in Fig. 2, with the observing information collected in Table 1.

To obtain radial velocities (RVs) of the primary, we normalized

Table 1. Spectroscopic observation log of α Dra.

UTC Date (yy/mm/dd)	BJD (day)	Orbital phase	SNR	RV (km/s)
2019-10-28	2458785.3134	0.475	86	4.4 ± 0.1
2019-11-01	2458788.7821	0.543	103	26.7 ± 0.1
2019-11-17	2458804.6782	0.852	115	−29.5 ± 0.1
2019-11-25	2458812.7061	0.008	59	−41.0 ± 0.2
2019-11-28	2458815.6997	0.066	138	−40.3 ± 0.1
2019-11-29	2458816.7830	0.087	128	−40.2 ± 0.2
2019-11-30	2458817.6497	0.104	119	−39.8 ± 0.2
2019-12-01	2458818.6397	0.123	127	−39.0 ± 0.1
2019-12-04	2458821.6927	0.183	145	−36.4 ± 0.1
2019-12-08	2458825.6532	0.260	107	−30.7 ± 0.1
2019-12-10	2458827.6502	0.298	117	−26.6 ± 0.1
2019-12-11	2458828.6200	0.317	114	−24.8 ± 0.1
2019-12-12	2458829.7898	0.340	112	−21.8 ± 0.1
2019-12-13	2458830.6016	0.356	93	−19.7 ± 0.1
2019-12-14	2458831.6115	0.376	127	−16.7 ± 0.1
2019-12-20	2458837.6224	0.492	121	9.2 ± 0.1
2019-12-21	2458838.6407	0.512	140	15.7 ± 0.1
2019-12-22	2458839.5728	0.530	113	22.0 ± 0.1
2020-01-04	2458852.7108	0.786	122	−13.5 ± 0.1
2020-01-05	2458853.5553	0.802	123	−18.5 ± 0.1
2020-01-06	2458854.5305	0.821	107	−23.7 ± 0.1
2020-01-12	2458860.5458	0.938	115	−38.7 ± 0.1
2020-01-13	2458861.5191	0.957	111	−39.8 ± 0.1
2020-01-15	2458863.5105	0.996	96	−40.8 ± 0.1
2020-01-16	2458864.5086	0.015	108	−41.1 ± 0.1
2020-01-17	2458865.5024	0.035	125	−41.1 ± 0.1
2020-01-18	2458866.5237	0.054	112	−41.3 ± 0.1
2020-01-18	2458867.4961	0.073	105	−40.6 ± 0.1
2020-01-24	2458872.5447	0.172	129	−37.0 ± 0.1
2020-01-26	2458874.5474	0.210	151	−34.7 ± 0.1
2020-01-27	2458875.5441	0.230	125	−33.2 ± 0.1
2020-01-28	2458876.5452	0.249	149	−31.7 ± 0.1
2020-01-29	2458877.5674	0.269	111	−29.9 ± 0.1
2020-01-30	2458878.5294	0.288	109	−28.3 ± 0.1
2020-01-31	2458879.5290	0.307	98	−26.0 ± 0.1
2020-02-01	2458880.7203	0.331	105	−23.1 ± 0.1
2020-02-02	2458881.5312	0.346	127	−21.2 ± 0.1
2020-02-06	2458885.5133	0.424	94	−7.7 ± 0.1
2020-02-07	2458886.5115	0.443	116	−3.9 ± 0.1
2020-02-08	2458887.5069	0.463	149	0.9 ± 0.1
2020-02-09	2458888.8044	0.488	142	7.7 ± 0.1
2020-02-10	2458889.7604	0.506	151	13.3 ± 0.1
2020-02-11	2458890.5264	0.521	115	18.4 ± 0.1
2020-02-12	2458891.5308	0.541	133	25.6 ± 0.1
2020-02-13	2458892.5064	0.560	76	32.9 ± 0.1
2020-02-14	2458893.5199	0.579	135	41.1 ± 0.1
2020-02-15	2458895.4958	0.618	101	53.3 ± 0.3
2020-02-16	2458896.4804	0.637	108	55.1 ± 0.3
2020-02-17	2458897.4926	0.657	101	52.2 ± 0.3
2020-02-18	2458898.4802	0.676	148	44.6 ± 0.1
2020-02-19	2458899.4838	0.695	148	33.5 ± 0.1
2020-02-21	2458901.4682	0.734	124	10.8 ± 0.1
2020-02-22	2458901.5144	0.735	130	10.4 ± 0.1
2020-02-22	2458901.5577	0.736	146	9.9 ± 0.1
2020-02-22	2458901.5873	0.736	136	9.6 ± 0.1
2020-02-22	2458901.6165	0.737	138	9.3 ± 0.1
2020-02-22	2458901.6418	0.737	127	8.7 ± 0.1
2020-02-22	2458901.6738	0.738	129	8.1 ± 0.1
2020-02-22	2458901.6937	0.738	131	7.7 ± 0.1

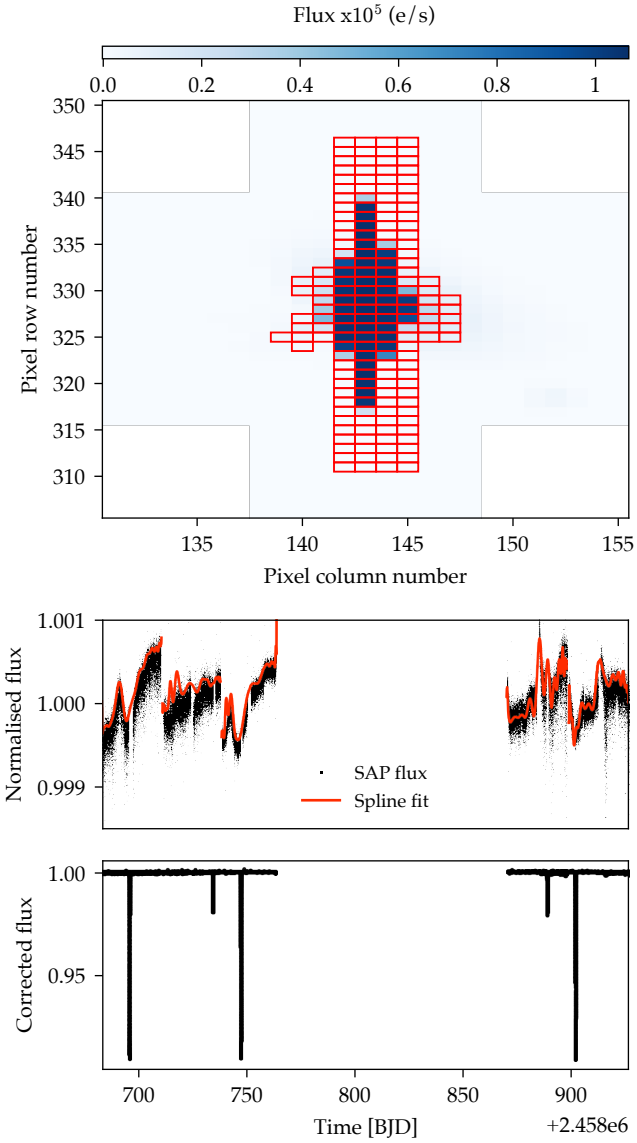

Figure 1. Top: The *TESS* target pixel file of α Dra for the first sector in which it was observed (14). The highlighted grey area shows the pixels used to produce the simple aperture photometry light curve from the *TESS* pipeline. Middle: The uncorrected flux with eclipses removed. The red lines are the spline fits. Bottom: The final corrected light curve after dividing through by the spline fit, with the eclipses included.

the spectra to the continuum by fitting a third-order polynomial to the upper 95th percentile of each spectral order. We then divided the flux of each order by this fit, and re-sampled the spectra to a constant log wavelength step of 0.02 Å, ensuring that the spectra are equally spaced in velocity steps. The orders of each spectrum were then merged and cross-correlated against the first spectrum in the series (a 'template' spectrum). RVs were then derived from this cross-correlation by fitting a 1D Gaussian curve between −200 and 200 km/s. From these initial RVs, we constructed a refined template spectrum by shifting and stacking all 61 spectra to the primary reference frame. We repeated the cross-correlation for the new template spectrum, constructing a new template at each iteration until the difference between the current and previous extracted RVs was less than 0.01 m/s. We then converted the relative RVs to absolute RVs by cross-correlating the final primary template spectrum with an atomic linelist bundled with the iSpec software (Blanco-Cuaresma et al. 2014) generated for an A0 type star. We extracted the radial velocities only within the wavelength regions between 5030 to 5350 Å, which we found to have the sharpest absorption lines.

α Dra is well known to be SB1, so only the fractional radii (R/a) can be determined from a combined light curve and RV analysis. To measure the absolute radii of the components requires RV measurements of the secondary, which would allow us to constrain the semi-major axis of the orbit. We thus attempted to find spectral lines from the secondary by shifting and stacking the spectra to the reference frame of the primary. We constructed a high SNR primary spectrum by taking the median spectrum of all shifted and stacked spectra. This spectrum was then subtracted from each individual spectrum, which were then cross-correlated with each other to show possible variations caused by the secondary. While we observed some residual signal in the cross-correlation, we were unable to derive radial velocities of the secondary star. This is not surprising – Behr et al. (2009) suggests that the secondary star accounts for less than 15% of the total luminosity of the system. This estimate agrees with direct interferometric measurement of a 1.83 ± 0.07 mag difference at $\lambda = 7000$ Å by Hutter et al. (2016). Additionally, Kallinger et al. (2004) found that the signature of the secondary is only marginally visible. Using the high-quality *SOPHIE* spectrum we found a possible contribution of the secondary star in the vicinity of the strongest metal lines (Ca II 3933, Mg II 4481 Å) (Fig. 3). These faint and broad features, indicating the secondary's $v \sin i \sim 200$ km s^{-1}, are red-shifted relative to the primary, which agrees with the orbital solution derived below. However, these lines are too faint to be reliably measured in the lower SNR *SONG* spectra.

We then attempted to disentangle the spectra using two independent spectral disentangling routines to obtain the signal for the secondary component. The first technique employed is a grid based iterative shift and stack routine (for an in depth discussion see e.g. Pavlovski & Hensberge 2010; Mahy et al. 2012; Shenar et al. 2020). As described above, this process involves first shifting all of the spectra to the reference of the primary and constructing a high SNR primary spectrum and then subtracting it from each individual spectrum. In this case however, instead of calculating a cross-correlating the residual spectra, we shifted all of the residual spectra to the reference of the secondary based on an assumed secondary semi-amplitude. A secondary spectrum was then constructed and subtracted from the original individual spectrum, and then this process was continued iteratively until the changes between iterations were negligible. A χ^2 value was then determined by reconstructing the individual spectra from the disentangled primary and secondary spectra and comparing the reconstructed spectra to the observations. This was done over a grid of secondary semi-amplitudes in order to find an optimal secondary semi-amplitude. While there was some structure in the χ^2 of the secondary semi-amplitude, the resulting secondary spectra did not show any discernible stellar features. The second technique employed is FDBinary (Ilijic et al. 2004), which unlike the shift and stack technique, operates in Fourier space (for an in depth discussion see e.g. Hadrava 1995; Ilijic et al. 2004; Pavlovski & Hensberge 2010). Based on a subset of orbital parameters, the remaining unknown orbital parameters can be determined. In this case, we left the semi-amplitude of the secondary free and let FDBinary optimize it. As with the iterative shift and stack, the resulting spectrum did not show any discernible stellar features.

Finally, we attempted to increase the signature of the secondary by applying Least-Squares Deconvolution (LSD) to the *SONG* spectra. In brief, this method builds an average, deconvolved line profile

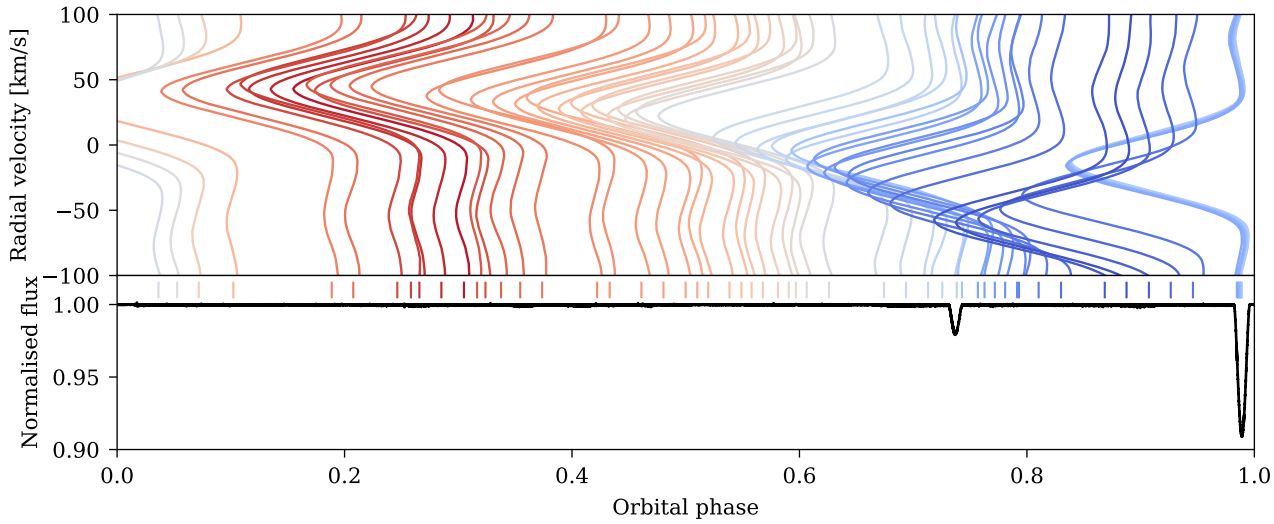

Figure 2. Top: Cross-correlation of each *SONG* spectrum against the constructed template. Each cross-correlation is coloured by its Doppler shift. Bottom: *TESS* light curve of α Dra folded on the orbital period. The coloured vertical lines above the light curve indicate orbital phases where *SONG* spectra were obtained.

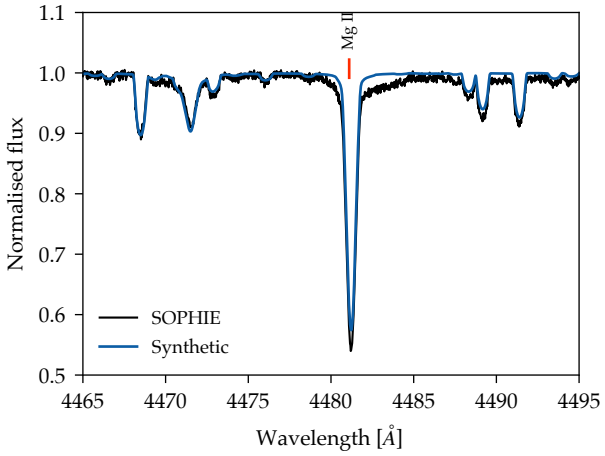

Figure 3. *SOPHIE* spectrum of α Dra in black with the best-fitting spectrum obtained in section overlaid in red. The broad feature near the Mg II line (4481 Å) is potentially caused by the rapidly rotating secondary.

of all the lines within a given wavelength range from a selected line mask (Donati et al. 1997). While the classical LSD methodology relies on a single mask and single component to the average profile, we use the generalised LSD approach introduced by Tkachenko et al. (2013), which allows for the computation of multiple stellar components from the same spectrum using different line lists. In this way, we can compute the average profile of each component without compromising or suppressing the signal of the other component. We computed the LSD profiles for two stellar components using three LSD components each, from 4290 Å to 5600 Å. We used a synthetic line list computed from the Vienna Atomic Line Database (VALD-II, Kupka et al. 1999), using the atmospheric parameters derived in Sec. 4. Similar to our other attempts, we could not reliably detect the presence of the secondary in the LSD profiles, despite the expected ~15% light contribution.

3 BINARY MODELLING

We simultaneously modelled the *TESS* photometry and radial velocity measurements to determine the fundamental parameters of the system. To perform the fit, we utilised the ELLC eclipsing binary code (Maxted 2016), wrapped in the Markov Chain Monte Carlo (Goodman & Weare 2010) ensemble sampling code: EMCEE (Foreman-Mackey et al. 2013). We supplemented our radial velocity data with that of Bischoff et al. (2017), which greatly increased the precision on the orbital period.

3.1 ELLC setup

The free parameters in our model were: the orbital period ($P_{\rm orb}$), the sum of the fractional radii ($r_{\rm sum} = (R_1 + R_2)/a$, where a is the semi-major axis of the orbit), the ratio of radii (R_2/R_1), the orbital inclination (i), reference time of primary eclipse (T_0), the surface brightness ratio averaged over both stellar disks in the TESS band (S_T), the semi-major axis of the primary (a_1), the eccentricity (e) and periapsis (ω) parametrised such that $f_c = \sqrt{e}\cos\omega$ and $f_s = \sqrt{e}\sin\omega$, the systemic velocity for each RV data-set ($\gamma_{v,(\alpha,\beta)}$), and the quadratic limb-darkening parameters ($q_{i,j}$). Priors on the eccentricity, time of primary eclipse, orbital period, and periapsis were chosen to be a narrow uniform prior centred around the values from Bischoff et al. (2017). For the limb-darkening parameters, we used the efficient sampling method from Kipping (2013) with uniform priors between 0 and 1.

Before sampling our model with EMCEE, we examined whether we could extract mass and temperature information from the light curve. For α Dra, the *TESS* photometry exhibits clear v-shaped eclipses indicative of a grazing eclipsing system. In a detached binary with grazing eclipses, the light curve is insensitive to the mass and temperature ratios. Photometric mass ratios can be determined accurately for completely eclipsing binaries, which break the degeneracy between the radii and inclination (Terrell & Wilson 2005). Photometric mass ratios can also be obtained for short-period binaries with ellipsoidal variations (i.e., contact and overcontact binaries). However, for a detached grazing system with no out-of-

eclipse variability, the mass ratio only indirectly affects the limb darkening values used. We utilised a limb-darkening lookup table produced by Claret (2017) generated with the PHOENIX atmosphere models (Husser et al. 2013) for a square root limb-darkening law to attempt to fit the temperature and mass of both stars. In practice, however, the limb-darkening coefficients vary by less than 0.1% in the temperature region of interest. We performed a linear interpolation on the table and attempted to fit the light curve by adjusting the temperature and masses of the components. We found the result to be very poorly constrained, so we chose not to attempt a fit for temperature and mass in the model.

There is a clear anomaly in the radial velocity measurements during primary eclipse (inset of Fig. 5) which we attribute to the Rossiter-McLaughlin (RM) effect. We fitted for this in the ELLC model by allowing the projected rotational velocity, $v \sin i$, to be a free parameter. For the primary star, we used a narrow Gaussian prior on $v \sin i$ of $N \sim (26.2, 0.2)$ which was taken from spectral analysis performed by Gray (2014). We did not collect enough spectra during secondary eclipse to detect the RM effect for the secondary.

Recent work has shown that significant degeneracies exist in the parameter space of eclipsing binary models (Conroy et al. 2020). Such degeneracies often lead to sampling of a local minimum as opposed to the correct parameter values. To avoid this, we initialised the parameters for sampling by using a differential evolution algorithm, which aims to find the global minimum of the parameter space (Storn & Price 1997). Differential evolution is a costly algorithm which requires many evaluations of the model, so we only applied it to every 20th data point in the in-eclipse light curve. We used several other techniques to speed-up computation as follows. Since the system is fully detached, we modelled both components as spheres. We further fitted only the in-eclipse flux data since the light curve is essentially constant out of eclipse. After obtaining a good initial fit, we ran the EMCEE sampler with 70 walkers for 15,000 steps, with 10,000 steps of burn-in. After sampling, we found that the final values were almost identical to the initial values used.

3.2 Results

We show the best fitting models in Fig. 4 and Fig. 5 for the light and radial velocity curves, respectively, and corner plots of the directly sampled parameters in Appendix A1. The median value of the posterior probability for each parameter is reported in Table 2, along with uncertainties reported at their 16th and 84th percentiles. From Fig. 4, there is clearly some eclipse-to-eclipse variability that is not accounted for by the light curve model. We tried several techniques to account for this, including fitting for apsidal motion, fixing the limb-darkening parameters to set values, and re-processing the target pixel file with other methods. However, we were unable to remove the residual signal. We believe its most likely origin is either a background star that was included by the aperture mask, or red noise inherent in the *TESS* data, because the shape of the eclipse changes marginally every orbital period. Since the residual flux is less than 0.002% of the total flux, it is unlikely to strongly affect the resulting parameters.

4 ANALYSIS OF THE PRIMARY

We determined the effective temperature ($T_{\rm eff}$) and surface gravity ($\log g$) of α Dra A using the UVBYBETA code developed by Napiwotzki et al. (1993). This code is based on the Moon & Dworetsky

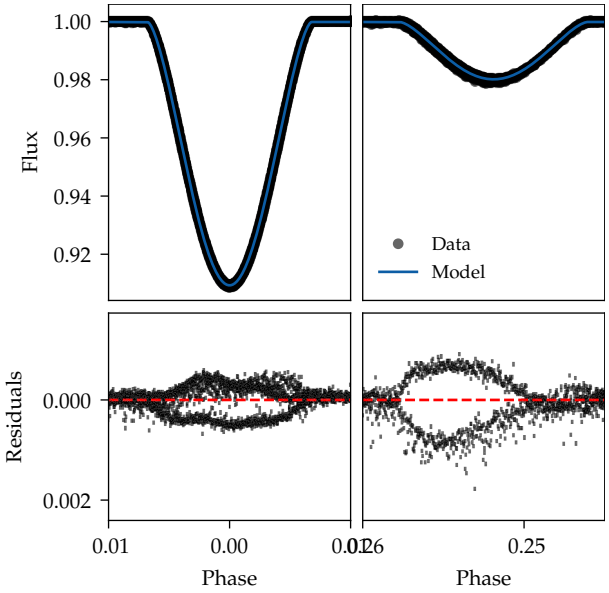

Figure 4. Fit to the light curve shown for the primary and secondary phase folded eclipses. Note that the phase has been corrected so that the primary eclipse occurs at a phase of 0.

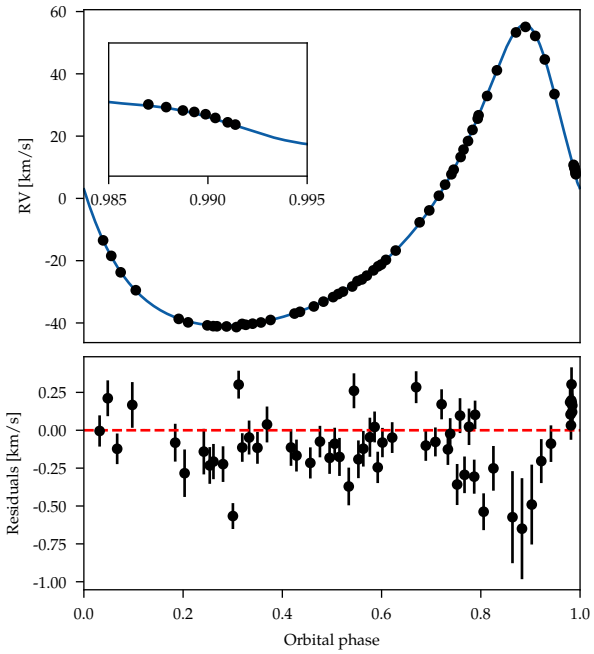

Figure 5. Fit to the primary stars' radial velocity curve. The top panel shows the data (black points) and best fitting model (blue line). The bottom panel shows the residual (observed minus calculated) scatter. Points are shown for the *SONG* RVs only.

(1985) grid, which calibrates the $uvby\beta$ photometry in terms of $T_{\rm eff}$ and $\log g$. The derived effective temperature is $T_{\rm eff} = 9975 \pm 125$ K and $\log g = 3.63 \pm 0.20$ dex.

We also modelled the photometry by fitting to MIST stellar isochrones with the ISOCHRONES package (Morton 2015). We simultaneously fit a combination of Gaia, WISE, 2MASS, and Strömgren photometry, using a Markov chain Monte-Carlo nested sampling approach to find the best-fitting atmospheric parameters (PyMultinest; Buchner et al. 2014). Uncertainties on the constraints were included

Parameter	Prior	Value	Unit
$P_{\rm orb}$	U~(50.4, 52.4)	$51.41888^{+0.00008}_{-0.00008}$	day
$(R_1 + R_2)/a$	U~(0.01, 0.1)	$0.0705^{+0.0005}_{-0.0004}$	
R_2/R_1	U~(0.1, 0.9)	$0.47^{+0.01}_{-0.01}$	
S_T	U~(0.01, 1.5)	$1.03^{+0.04}_{-0.03}$	
i	U~(45, 90)	$86.35^{+0.04}_{-0.04}$	deg
T_0	U~(1695, 1697)	$2458696.0199^{+0.0002}_{-0.0002}$	BJD
f_c	U~(0.5, 0.7)	$0.6068^{+0.0003}_{-0.0003}$	
f_s	U~(0.07, 0.3)	$0.237^{+0.002}_{-0.001}$	
a_1	U~(10, 150)	$44.564^{+0.105}_{-0.106}$	$R_\odot$
$\gamma_{V,\alpha}$	U~(-20, -5)	$-11.68^{+0.03}_{-0.03}$	km/s
$\gamma_{V,\beta}$	U~(-20, -5)	$-13.5^{+0.1}_{-0.1}$	km/s
$v \sin i$	N~(26.2, 0.2)	$27.6^{+0.3}_{-0.6}$	km/s
q_{11}	U~(0.0, 1.0)	$0.2^{+0.1}_{-0.1}$	
q_{12}	U~(0.0, 1.0)	$0.5^{+0.3}_{-0.3}$	
q_{21}	U~(0.0, 1.0)	$0.2^{+0.2}_{-0.1}$	
q_{22}	U~(0.0, 1.0)	$0.5^{+0.3}_{-0.3}$	
Quantities			
R_1/a		$0.0479^{+0.0003}_{-0.0002}$	
R_2/a		$0.0226^{+0.0005}_{-0.0005}$	
K_1		$47.74^{+0.06}_{-0.06}$	km/s
$f\,(M_1, M_2)$		$0.438^{+0.002}_{-0.002}$	$M_\odot$
e		$0.4242^{+0.0003}_{-0.0003}$	
ω		$0.3718^{+0.0024}_{-0.0022}$	rad

Table 2. All parameters used in the combined photometric and radial velocity model, including their priors. The reported values are the median result of the MCMC chain, with errors reported as the 16th and 84th percentiles of the posterior distribution. The derived quantities are parameters that were obtained purely from these parameters (i.e., the eccentricity is the sum of the squares of f_c and f_s). Note that the time of primary eclipse was sampled in Barycentric *TESS* Julian Date (BJD - 2457000). We report the posterior value in BJD for convenience.

as priors in the Bayesian fitting process and were thus propagated to the final results. We attempted to fit both a single and a binary star isochrone model using the UVBYBETA-derived temperature and surface gravity as priors, and also using the Gaia DR2 parallax of 12.18 ± 0.31 mas (Gaia Collaboration et al. 2018). Fitting the photometry as a binary system yielded no useful results. Indeed, this is not unexpected because the secondary only accounts for around 15% of the total flux of α Dra. On the other hand, the single star fit was well-constrained by the tight priors on temperature and surface gravity, and yielded the mass and radius of the primary to be $3.45^{+0.13}_{-0.11}$ $M_\odot$ and $5.14^{+0.14}_{-0.13}$ $R_\odot$ respectively. The log luminosity of the system was also found to be $2.385^{+0.03}_{-0.02}$ $L_\odot$.

It has previously been suggested that α Dra A is photometrically variable, with a period of about 53 min and an amplitude of 1-2 mmag (Kallinger et al. 2004). It was speculated that α Dra could belong to the unconfirmed class of so-called 'Maia variables', lying between the blue edge of the instability strip of δ Scuti stars and the red edge of slowly pulsating B-type stars (White et al. 2017). As found by Bedding et al. (2019), we see no evidence for photometric variability in α Dra (beyond eclipses), and can rule out variability on timescales shorter than 8 hr at the precision of 10 parts per million (ppm) from the eclipse subtracted light curve.

4.1 Abundance analysis

To determine elemental abundances, we retrieved previous observations of α Dra from the *SOPHIE* archive hosted at Observatoire de Haute Provence. *SOPHIE* is an échelle spectrograph that, in its high resolution mode (R = 75000), yields a full spectral coverage from 3820 Å to 6930 Å in 39 orders (Perruchot et al. 2008). We chose to analyse the *SOPHIE* spectrum as opposed to the newly collected *SONG* spectra since *SOPHIE* posseses a wider spectral coverage at a higher SNR. The spectra were extracted online from the detector images using a pipeline adapted from the High Accuracy Radial Velocity Planet Searcher (HARPS). We normalized each reduced order separately using a Chebyshev polynomial fit with sigma clipping, rejecting points above or below one standard deviation of the local continuum. Normalized orders were then merged, corrected by the blaze function, and re-sampled into a constant wavelength step of 0.02 Å (see Royer et al. 2014, for more details).

Atomic linelists from Kurucz's database provided the basis to construct our linelist. These lists collect data mostly from the literature for light and heavy elements, usually critically evaluated transition probabilities from Martin et al. (1988) and Fuhr et al. (1988), and computed data by Kurucz (1992a) for the iron group elements. A first linelist was built from Kurucz's gfall21oct16.dat[1] which includes hyperfine splitting levels. We then updated several oscillator strengths and damping parameters with more recent and accurate determinations when necessary. As a rule, we have preferred NIST[2] and Wiese et al. (1996) oscillator strengths for CNO and also Nilsson et al. (2006). The H I lines are calculated using Vidal et al. (1973) tables upgraded by Schoening & Butler up to H 10. The He I lines are computed in SYNSPEC49 by using specific tables, either from Shamey (1969) or Dimitrijevic & Sahal-Brechot (1984).

We introduced hyperfine components for a few lines of Mn II (Holt et al. 1999), isotopic and hyperfine transitions for a few lines of Ga II (Nielsen et al. 2000). To model the Hg II line at 3983.93 Å, we have included 9 hyperfine transitions from the various isotopes from Hg^{196} up to Hg^{204} from Dolk et al. (2003). For the Rare Earths, we retrieved all relevant transitions from the DREAM database[3]. We also used specific publications reporting on laboratory measurements: Sm II (Lawler et al. 2006), Nd II (Den Hartog et al. 2003), Eu II (Lawler et al. 2001b), Tb II (Lawler et al. 2001a). The presence of these heavy elements was considered given that α Dra has parameters similar to HgMn and Ap stars, but no definitive identification of these elements was made.

In Kurucz's linelists, the damping constants are taken from the literature when available. For the iron group elements, they come from Kurucz (1992b) computations. Additional damping constants for a few Si II lines were taken from Lanz et al. (1988). When they are not available from the linelist, damping constants are actually computed in SYNSPEC49 using an approximate formula (Kurucz & Avrett 1981).

We derived the abundances of 21 chemical elements by iteratively adjusting synthetic spectra to the normalized spectrum and looking for the best fit to carefully selected unblended lines. Synthetic spectra were computed assuming LTE using Hubeny & Lanz (1992) SYNSPEC49 code, which calculates lines for elements up to Z=99. In order to derive the microturbulent velocity, we simultane-

[1] http://kurucz.harvard.edu/linelists/gfnew/gfall21oct16.dat
[2] http://physics.nist.gov/cgi-bin/AtData/linesform
[3] http://www.umh.ac.be/astro/dream.shtml

Table 3. Atmospheric composition of the primary star of α Dra. We here refer to the absolute abundance in the star: $\log_{10}\left(\frac{\mathrm{X}}{\mathrm{H}}\right)_\star$. The third column shows the corresponding solar abundance.

Ion	Absolute abundance	Solar abundance
He	−1.17 ± 0.45	−1.070
C	−3.63 ± 0.34	−3.61
O	−3.22 ± 0.19	−3.34
Na	−5.67 ±,0.20	−5.67
Mg	−4.47 ± 0.29	−4.42
Al	−5.53 ± 0.20	−5.53
Si	−4.60 ± 0.09	−4.45
P	−6.55 ± 0.16	−6.55
S	−4.67 ± 0.16	−4.67
Ca	−5.79 ± 0.17	−5.64
Sc	−9.23 ± 0.20	−8.83
Ti	−6.92 ± 0.06	−6.98
V	−7.56 ± 0.23	−8.00
Cr	−6.25 ± 0.17	−6.33
Mn	−6.61 ± 0.08	−6.61
Fe	−4.60 ± 0.16	−4.50
Ni	−6.35 ± 0.27	−5.75
Sr	−9.55 ± 0.20	−9.03
Y	−9.16 ± 0.20	−9.16
Zr	−9.40 ± 0.20	−9.40
Ba	−9.87 ± 0.22	−9.87

ously derived the iron abundance [Fe/H] for fifty unblended Fe-II lines and a set of microturbulent velocities ranging from 0.0 to 2.0 km/s. The adopted microturbulent velocity is the value which minimizes the standard deviations, that is, for that value, all Fe-II lines yield the same iron abundance. We found a null microturbulent velocity, a result consistent with the value found by Adelman et al. (2011).

4.2 Model atmospheres

The ATLAS9 code (Kurucz 1992b) was used to compute a first model atmosphere for the effective temperature and surface gravity of α Dra A ($T_{\rm eff}$=9975 K and log g=3.63 obtained with UVBYBETA) assuming a plane parallel geometry, a gas in hydrostatic and radiative equilibrium and local thermodynamical equilibrium. The ATLAS9 model atmosphere contains 72 layers with a regular increase in $\log \tau_{\rm Ross} = 0.125$ and was calculated assuming a solar chemical composition (Grevesse & Sauval 1998). It was converged up to $\log \tau = -5.00$ in order to attempt reproduce the cores of the Balmer lines. This ATLAS9 version uses the new opacity distribution function of Castelli & Kurucz (2004) computed for that solar chemical composition. Once a first set of elemental abundances were derived using the ATLAS9 model atmosphere, the atmospheric structure was recomputed for these abundances using the opacity sampling ATLAS12 code (Kurucz 2013). Slightly different abundances were then derived and a new ATLAS12 model was recomputed until the abundances in subsequent iterations differed by less than ± 0.10 dex.

We used only unblended lines to derive the abundances. For a given element, the final reported abundance is a weighted mean of the abundances derived for each transition (the weights are derived from the NIST grade assigned to that particular transition). For several elements, in particular the heaviest elements, only one unblended line was available and the abundance should be regarded as uncertain. For each modelled transition, the adopted abundance is that which provided the best fit calculated with SYNSPEC49 to the observed normalized profile. A grid of synthetic spectra was computed with SYNSPEC49 (Hubeny & Lanz 1992) to model each chosen unblended line of the 21 elements. Computations were iterated by varying the unknown abundance until minimization of the χ^2 between the observed and synthetic spectrum was achieved. The final abundances of α Dra are listed in Table 3.

5 DISCUSSION AND CONCLUSIONS

A0 III is a rare spectral type. It has been suggested to be a transitional state between two types of chemically peculiar A stars (Adelman 1987). As a result, it is challenging to determine fundamental parameters. To the best of our knowledge, only two other eclipsing binaries are known to host A0 III type stars: V452 Mon (Sebastian et al. 2012) and V1461 Aql (Houk & Swift 1999).

Given the obtained mass function and mass of the primary, we estimate the secondary to have a minimum mass of around 2.50 ± 0.14 $M_\odot$, which corresponds to an A2V spectral type with a luminosity of around L = 40 $L_\odot$. This is in very good agreement with the known secondary contribution of 15.6% to the total flux of α Dra. The fact that the secondary remains undetected in the spectra could be explained by a rapid rotational velocity. If the secondary is an A-type star, as suggested by the mass function, then it is likely to have a high $v \sin i$ which would lead to broadening of the spectral lines, as seen in Fig. 3. Using the results of (Southworth et al. 2007), we can also est imate the surface gravity of the secondary from the orbital period (P), the RV semi-amplitude of the primary (K_1), eccentricity (e), inclination (i), and fractional radius of the secondary (R_2/a):

$$g = \frac{2\pi}{P} \frac{(1-e^2)^{1/2} K_1}{(R_2/a)^2 \sin i}. \quad (1)$$

Using this, we find the surface gravity of the secondary to be 4.08 ± 0.02.

The derived abundances for α Dra A are clearly non-solar. Most elements are under-abundant by factors ranging from 0.80 down to 0.30 times the solar value. Only vanadium is found to be over-abundant, by a factor of almost 3, while aluminium, sulphur, manganese, yttrium and barium have solar abundances. The overall deficiency of several elements agrees roughly with the under-abundances found for many elements by Adelman et al. (2001) but the under-abundances we find are usually less pronounced than in their work. The helium and iron under-abundances agree reasonably well with their determinations. The overall metal deficiency of α Dra A is thus confirmed. Whether this deficiency was present at the formation of the star or is the result of stellar evolution remains an open question.

Future measurements of this system could improve the precision on the fundamental properties. Interferometry to obtain the angular diameters of both systems would yield the semi-major axis of the orbit and the mass ratio. If the secondary RVs could be extracted, almost all parameters in the system could be obtained. Finally, a complete astrometric orbit is expected from the impending release of Gaia DR3. This would provide independent measures of the mass ratio, radii, and semi-major axis of the orbit.

ACKNOWLEDGEMENTS

We are grateful to the *TESS* team for such excellent data. We thank Andrej Prsa for useful discussions. DRH gratefully acknowledges

the support of the Australian Government Research Training Program (AGRTP) and University of Sydney Merit Award scholarships. This research has been supported by the Australian Government through the Australian Research Council DECRA grant number DE180101104 and Discovery Project DP210103119. This research used observations made with the Hertzsprung *SONG* telescope operated on the Spanish Observatorio del Teide on the island of Tenerife by the Aarhus and Copenhagen Universities and by the Instituto de Astrofisica de Canarias. Funding for the Stellar Astrophysics Center is provided by The Danish National Research Foundation (Grant agreement no. DNRF106). This work has made use of the VALD database, operated at Uppsala University, the Institute of Astronomy RAS in Moscow, and the University of Vienna. CJ has received funding from the European Research Council (ERC) under the European Union's Horizon 2020 research and innovation programme (grant agreement N°670519: MAMSIE) and from the Research Foundation Flanders (FWO) under grant agreement and G0A2917N (BlackGEM).

This paper has made use of the following software not cited in the text: NUMPY (Oliphant 2015), SCIPY (Virtanen et al. 2019), ASTROPY (Price-Whelan et al. 2018), and LIGHTKURVE (Vinícius et al. 2018).

REFERENCES

Adelman S. J., Caliskan H., Kocer D., Kablan H., Yüce K., Engin S., 2001, Astronomy and Astrophysics, 371, 1078

Adelman S. J., Yu K., Gulliver A. F., 2011, Astronomische Nachrichten, 332, 153

Andersen J., 1991, The Astronomy and Astrophysics Review, 3, 91

Andersen M. F., et al., 2014, 45, 83

Andersen M. F., et al., 2019, Astronomy & Astrophysics, 623, L9

Bedding T. R., Hey D. R., Murphy S. J., 2019, Research Notes of the AAS, 3, 163

Behr B. B., Hajian A. R., Cenko A. T., Murison M., McMillan R. S., Hindsley R., Meade J., 2009, The Astrophysical Journal, 705, 543

Bischoff R., et al., 2017, Astronomische Nachrichten, 338, 671

Blanco-Cuaresma S., Soubiran C., Heiter U., Jofré P., 2014, Astronomy & Astrophysics, 569, A111

Buchner J., et al., 2014, Astronomy & Astrophysics, 564, A125

Campbell W. W., Curtis H. D., 1903, The Astrophysical Journal, 18

Castelli F., Kurucz R. L., 2004, arXiv:astro-ph/0405087

Claret A., 2017, Astronomy & Astrophysics, 600, A30

Conroy K. E., et al., 2020, The Astrophysical Journal Supplement Series, 250, 34

Den Hartog E. A., Lawler J. E., Sneden C., Cowan J. J., 2003, The Astrophysical Journal Supplement Series, 148, 543

Dimitrijevic M. S., Sahal-Brechot S., 1984, Astronomy and Astrophysics, 136, 289

Dolk L., Wahlgren G. M., Hubrig S., 2003, Astronomy and Astrophysics, 402, 299

Donati J.-F., Semel M., Carter B. D., Rees D. E., Collier Cameron A., 1997, Monthly Notices of the Royal Astronomical Society, 291, 658

Foreman-Mackey D., Hogg D. W., Lang D., Goodman J., 2013, Publications of the Astronomical Society of the Pacific, 125, 306

Fuhr J. R., Martin G. A., Wiese W. L., 1988, Journal of Physical and Chemical Reference Data, 17

Gaia Collaboration et al., 2018, Astronomy and Astrophysics, 616, A1

Goodman J., Weare J., 2010, Communications in Applied Mathematics and Computational Science, Vol. 5, No. 1, p. 65-80, 2010, 5, 65

Graczyk D., 2003, Monthly Notices of the Royal Astronomical Society, 342, 1334

Gray D. F., 2014, The Astronomical Journal, 147, 81

Grevesse N., Sauval A. J., 1998, Space Science Reviews, 85, 161

Hadrava P., 1995, Astronomy and Astrophysics Supplement Series, 114, 393

Holt R. A., Scholl T. J., Rosner S. D., 1999, Monthly Notices of the Royal Astronomical Society, 306, 107

Houk N., Swift C., 1999, Michigan Catalogue of Two-Dimensional Spectral Types for the HD Stars ; Vol. 5. Vol. 5, None

Hubeny I., Lanz T., 1992, Astronomy and Astrophysics, 262, 501

Husser T.-O., Wende-von Berg S., Dreizler S., Homeier D., Reiners A., Barman T., Hauschildt P. H., 2013, Astronomy and Astrophysics, 553, A6

Hutter D. J., Zavala R. T., Tycner C., Benson J. A., Hummel C. A., Sanborn J., Franz O. G., Johnston K. J., 2016, The Astrophysical Journal Supplement Series, 227, 4

Ilijic S., Hensberge H., Pavlovski K., Freyhammer L. M., 2004, 318, 111

Kallinger T., Iliev I., Lehmann H., Weiss W. W., 2004, Proceedings of the International Astronomical Union, 2004, 848

Kipping D. M., 2013, Monthly Notices of the Royal Astronomical Society, 435, 2152

Kupka F., Piskunov N., Ryabchikova T. A., Stempels H. C., Weiss W. W., 1999, Astronomy and Astrophysics Supplement Series, 138, 119

Kurucz R. L., 1992a, Revista Mexicana de Astronomia y Astrofisica, vol. 23, 23

Kurucz R. L., 1992b, Revista Mexicana de Astronomia y Astrofisica, vol. 23, 23

Kurucz R. L., 2013, Astrophysics Source Code Library, p. ascl:1303.024

Kurucz R. L., Avrett E. H., 1981, SAO Special Report, 391, 391

Lanz T., Dimitrijevic M. S., Artru M.-C., 1988, Astronomy and Astrophysics, 192, 249

Lawler J. E., Wickliffe M. E., Cowley C. R., Sneden C., 2001a, The Astrophysical Journal Supplement Series, 137, 341

Lawler J. E., Wickliffe M. E., Hartog E. A. D., Sneden C., 2001b, The Astrophysical Journal, 563, 1075

Lawler J. E., Den Hartog E. A., Sneden C., Cowan J. J., 2006, The Astrophysical Journal Supplement Series, 162, 227

Mahy L., Gosset E., Sana H., Damerdji Y., De Becker M., Rauw G., Nitschelm C., 2012, Astronomy and Astrophysics, 540, A97

Martin G. A., Fuhr J. R., Wiese W. L., 1988, New York: American Institute of Physics (AIP) and American Chemical Society, 1988

Maxted P. F. L., 2016, Astronomy & Astrophysics, 591, A111

Maxted P. F. L., et al., 2020, Monthly Notices of the Royal Astronomical Society, 498, 332

Moon T. T., Dworetsky M. M., 1985, Monthly Notices of the Royal Astronomical Society, 217, 305

Morton T. D., 2015, Astrophysics Source Code Library, p. ascl:1503.010

Napiwotzki R., Schoenberner D., Wenske V., 1993, Astronomy and Astrophysics, 268, 653

Nielsen K., Karlsson H., Wahlgren G. M., 2000, Astronomy and Astrophysics, 363, 815

Nilsson H., Ljung G., Lundberg H., Nielsen K. E., 2006, Astronomy and Astrophysics, 445, 1165

Oliphant T. E., 2015, Guide to NumPy, 2nd edn. CreateSpace Independent Publishing Platform, USA

Pavlovski K., Hensberge H., 2010, 435, 207

Perruchot S., et al., 2008, in Ground-Based and Airborne Instrumentation for Astronomy II. International Society for Optics and Photonics, p. 70140J, doi:10.1117/12.787379

Price-Whelan A. M., et al., 2018,] 10.3847/1538-3881/aabc4f, 156, 123

Renson P., Manfroid J., 2009, VizieR Online Data Catalog, 3260

Ricker G. R., et al., 2014, Journal of Astronomical Telescopes, Instruments, and Systems, 1, 014003

Royer F., et al., 2014, Astronomy and Astrophysics, 562, A84

Sebastian D., Guenther E. W., Schaffenroth V., Gandolfi D., Geier S., Heber U., Deleuil M., Moutou C., 2012, Astronomy and Astrophysics, 541, A34

Shamey L. J., 1969, PhD thesis

Shenar T., et al., 2020, Astronomy and Astrophysics, 639, L6

Smith J. C., et al., 2012, Publications of the Astronomical Society of the Pacific, 124, 1000

Southworth J., Wheatley P. J., Sams G., 2007, Monthly Notices of the Royal Astronomical Society, 379, L11

Storn R., Price K., 1997, Journal of Global Optimization, 11, 341
Terrell D., Wilson R., 2005, in Drechsel H., Zejda M., eds, , Zdeněk Kopal's Binary Star Legacy. Springer Netherlands, Dordrecht, pp 221–230, doi:10.1007/1-4020-3875-5_30
Tkachenko A., Reeth T. V., Tsymbal V., Aerts C., Kochukhov O., Debosscher J., 2013, Astronomy & Astrophysics, 560, A37
Torres G., Andersen J., Giménez A., 2010, Astronomy and Astrophysics Review, 18, 67
Vidal C. R., Cooper J., Smith E. W., 1973, The Astrophysical Journal Supplement Series, 25, 37
Vinícius Z., Barentsen G., Hedges C., Gully-Santiago M., Cody A. M., 2018,] 10.5281/zenodo.1181928
Virtanen P., et al., 2019, arXiv e-prints, 1907, arXiv:1907.10121
White T. R., et al., 2017, Monthly Notices of the Royal Astronomical Society, 471, 2882
Wiese W. L., Fuhr J. R., Deters T. M., 1996, Atomic transition probabilities of carbon, nitrogen, and oxygen : a critical data compilation. Edited by W.L. Wiese, J.R. Fuhr, and T.M. Deters. Washington, DC : American Chemical Society ... for the National Institute of Standards and Technology (NIST) c1996. QC 453 .W53 1996. Also Journal of Physical and Chemical Reference Data, Monograph 7. Melville, NY: AIP Press

APPENDIX A: CORNER PLOTS

This paper has been typeset from a TEX/LATEX file prepared by the author.

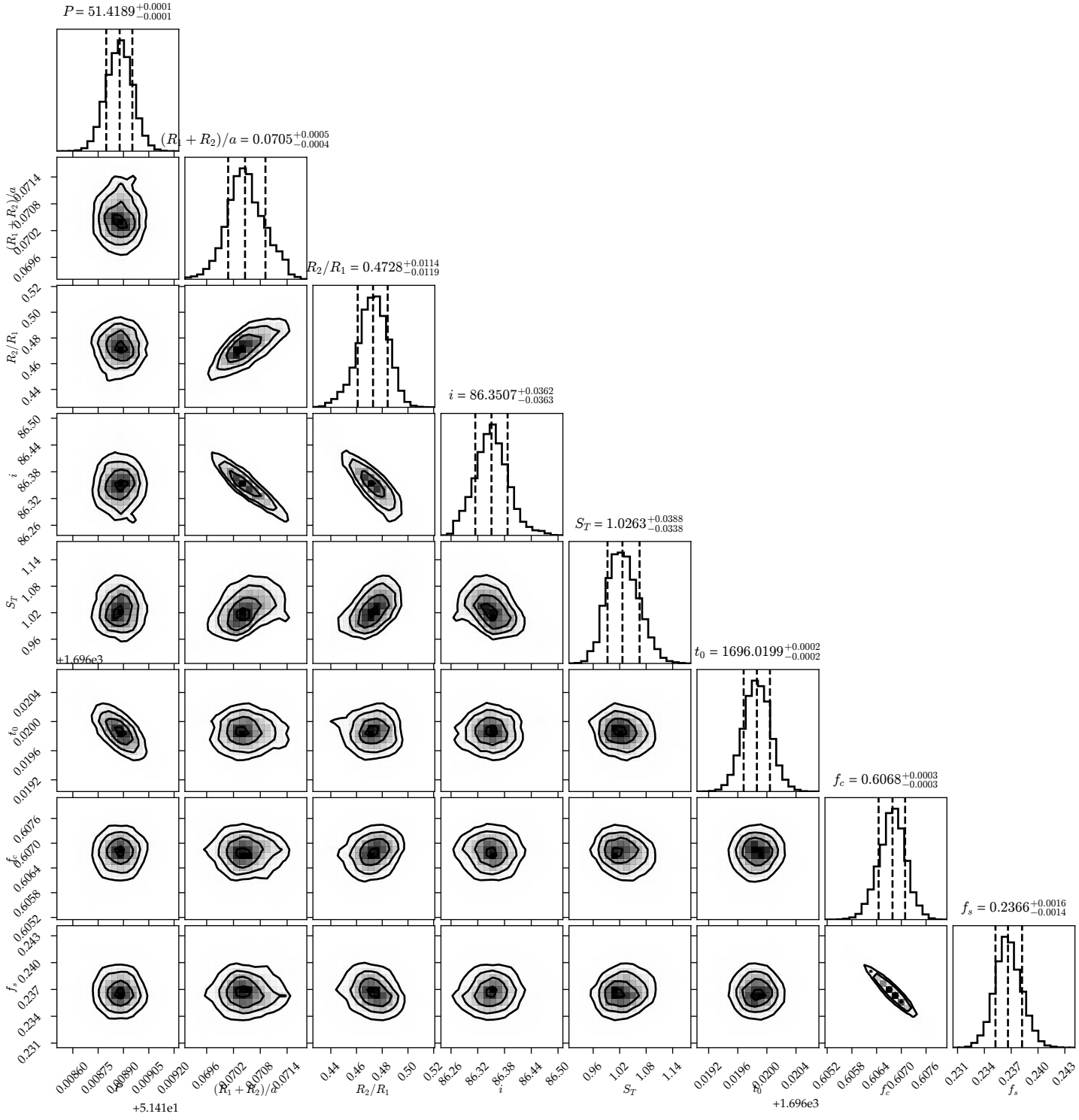

Figure A1. Corner plot of the posterior distributions for the combined light curve and RV model. The dashed black lines correspond to the 16th, 50th, and 84th percentiles. Note that t_0 was sampled in Barycentric *TESS* Julian Date (BTJD), corresponding to BJD - 2457000. Not all parameters in the model have been shown.